ADVANCED FUNCTIONAL MATERIALS
www.afm-journal.de

Morphological Origin of Charge Transport Anisotropy in Aligned Polythiophene Thin Films

Brendan T. O'Connor, Obadiah G. Reid, Xinran Zhang, R. Joseph Kline, Lee J. Richter, David J. Gundlach, Dean M. DeLongchamp,* Michael F. Toney, Nikos Kopidakis, and Garry Rumbles**

The morphological origin of anisotropic charge transport in uniaxially strain aligned poly(3-hexylthiophene) (P3HT) films is investigated. The macroscale field effect mobility anisotropy is measured in an organic thin film transistor (OTFT) configuration and compared to the local aggregate P3HT mobility anisotropy determined using time-resolved microwave conductivity (TRMC) measurements. The field effect mobility anisotropy in highly aligned P3HT films is substantially higher than the local mobility anisotropy in the aggregate P3HT. This difference is attributed to preferentially aligned polymer tie-chains at grain boundaries that contribute to macroscale charge transport anisotropy but not the local anisotropy. The formation of sharp grains between oriented crystalline P3HT, through tie chain removal by thermal annealing the strained aligned films, results in an order of magnitude drop in the measured field effect mobility for charge transport parallel to the strain direction. The field effect mobility anisotropy is cut in half while the local mobility anisotropy remains relatively constant. The local mobility anisotropy is found to be surprisingly low in the aligned films, suggesting that the π–π stacking direction supports charge carrier mobility on the same order of magnitude as that in the intrachain direction, possibly due to poor intrachain mobility through chain torsion.

1. Introduction

It is well known that the morphology of organic semiconductor films plays a significant role in dictating their electrical properties. In particular, anisotropic packing of organic semiconductors typically results in anisotropic charge transport properties, as has been demonstrated for a number of organic semiconductor materials.[1–12] In single crystal small molecule semiconductors such as rubrene, the anisotropy in charge transport can be directly related to the molecular packing structure and subsequent band structure.[13,14] In conjugated polymers, orienting the polymer long-axis to be primarily in one-direction has been shown to result in anisotropic charge transport for a number of polymers including poly(3-hexylthiphene) (P3HT),[1,11,15] poly[9,9′-dioctylfluorene-co-bithiophene] (F8BT),[4,16] and Poly[2,5-bis(3-tetradecylthiophen-2-yl) thieno[3,2-*b*]thiophene] (pBTTT),[3,6,12] among others.[2,17] In these films, it is typically found that charge transport is strongly favored in the direction of polymer backbone alignment over intermolecular paths, in agreement with theoretical predictions of mobility anisotropy in polymer crystals.[18,19] However, due to the semicrystalline nature of polymers, the origin of the mobility anisotropy may derive from characteristics of crystal packing, grain boundary character, inter-crystalline morphology, or a combination of these features.[20] The difficulty in determining the origin of the anisotropy is due in part to the practice of measuring the in-plane charge transport in an organic thin film transistor (OTFT) configuration where transport occurs across a channel that is commonly between 1 μm to 100 μm.[21] At these lengths the mobility is a convolution of transport through ordered and disordered regions of the film and likely follows a percolation pathway through the material along a path of least resistance.[22]

In this paper, we consider the mobility anisotropy from both local and macroscopic perspectives to improve our understanding of morphological characteristics that drive anisotropic electrical properties in aligned conjugated polymer films. We focus on the widely studied polymer, P3HT. Recently, straining

Prof. B. T. O'Connor
Department of Mechanical and Aerospace Engineering
North Carolina State University
Raleigh, NC 27695, USA
E-mail: btoconno@ncsu.edu
Dr. O. G. Reid, Dr. N. Kopidakis, G. Rumbles
Energy Sciences Division
National Renewable Energy Laboratory
Golden, CO 80401, USA
E-mail: garry.rumbles@nrel.gov
Dr. X. Zhang, Dr. R. J. Kline, Dr. L. J. Richter, Dr. D. M. DeLongchamp
Material Measurement Laboratory
National Institute of Standards and Technology
Gaithersburg, MD 20899, USA
E-mail: deand@nist.gov
Dr. D. J. Gundlach
Physical Measurement Laboratory
National Institute of Standards and Technology
Gaithersburg, MD 20899, USA
Dr. M. F. Toney
Stanford Synchrotron Radiation Lightsource
Menlo Park, CA 94025, USA

DOI: 10.1002/adfm.201303351

P3HT films on a polydimethylsiloxane (PDMS) substrate has been shown to be a simple and effective alignment method.[1] It was shown that as the film is uniaxially strained, the P3HT backbone preferentially aligns in the direction of strain. A major benefit of this approach is that the strain-aligned films can be transferred onto a number of substrates for detailed electrical and morphological characterization. In this paper we study the influence of intergrain morphology on charge transport by correlating morphological characterization with local and macroscale mobility measurements. We differentiate intergrain from intragrain transport characteristics by comparing macroscale field effect mobility measured in an OTFT configuration with the local charge mobility from time-resolved microwave conductivity (TRMC) measurements. This comparison shows the importance of polymer tie-chains bridging aggregates in facilitating charge transport, and suggests the mobility in the π–π stacking direction is similar in magnitude as that in the intrachain direction.

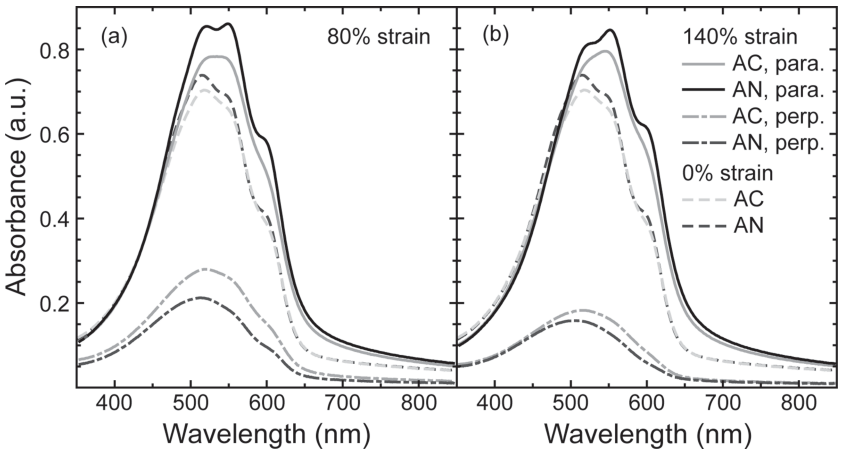

Figure 1. Absorbance spectrum for strained P3HT films. Films are measured under as-cast (AC) and thermally annealed (AN) conditions. The annealing conditions are 180 °C for 10 min. a) Films strained by 80% are compared to unstrained films. b) Films strained by 140% are compared to unstrained films.

2. Experimental Results

2.1. Morphology Characterization

The films are characterized using a suite of complementary tools that provide a relatively complete morphological picture.[23,24] These characterization tools include ultraviolet-visible (UV-vis) optical absorption spectroscopy, grazing incidence wide-angle X-ray diffraction (GIXD), small-angle X-ray scattering (GI-SAXS), atomic force microscopy (AFM), and transmission electron microscopy (TEM). Throughout film characterization we refer to P3HT aggregates and crystallites. We consider aggregates as a group of π-stacked conjugated segments that impart a specific optical absorption profile as discussed below, and crystallites as aggregates with enough interacting segments that allow for discernable X-ray diffraction peaks.[25] The crystallites are all considered aggregates, however not all aggregates will diffract.

The in-plane orientation of the polymer long-axis was characterized using UV-vis optical spectroscopy with polarized light. With the primary optical transition dipole moment (π–π^*) in P3HT parallel to the polymer backbone axis,[26] the average orientation of the polymer backbone can be determined by considering the absorbance anisotropy of the film. Uniaxially straining the film results in significant dichroism with absorbance being favored in the direction of strain, as shown in **Figure 1**. This is indicative of the polymer long-axis aligning in the direction of strain. Annealing the films at 180 °C for 10 min shows a slight increase in the dichroic ratio where the absorbance increases parallel to the strain direction and decreases in the perpendicular direction. To quantify the degree of alignment of the films, a 2D order parameter, $S_{2,\mathrm{mol}} = (R-1)/(R+1)$ is applied, where R is the dichroic ratio taken as the ratio of the peak absorbance for light polarized parallel to the strain direction to light polarized perpendicular to the strain direction.[1] Here, $S_{2,\mathrm{mol}} = 1$ for complete alignment and $S_{2,\mathrm{mol}} = 0$ for an isotropic distribution. The justification of using a 2D order parameter is given in the Supporting Information. The change in $S_{2,\mathrm{mol}}$ with strain and thermal annealing is given in **Figure 2**d. It is found that $S_{2,\mathrm{mol}} = 0.63$ ($R = 4.4$) for the 140% as-cast film and $S_{2,\mathrm{mol}} = 0.69$ ($R = 5.4$) for the annealed film. The uncertainty of the order parameter is expected to be within ±0.02 and primarily attributed to the uncertainty in the percent strain of the film.

In addition to the polymer backbone alignment, the vibronic features in the absorption spectrum provide information on the P3HT local order.[27–29] The character of the absorption arises from a complex interplay between intramolecular vibronic coupling and intermolecular, H-aggregate-like coupling. Previously, a weakly coupled H-aggregate model has been successfully applied to P3HT to quantitatively estimate the average conjugation length and quality of the aggregates in the film.[27–30] The absorption model fitting parameters include the free-exciton bandwidth (W), the Gaussian line width (σ), and the 0→0 transition energy (E_{00}). W can be interpreted in terms of the length of interacting chain segments forming the P3HT aggregates,[30] and σ a measure of the local interchain order. In addition to the P3HT local order, the absorption spectra are able to provide an estimate of the percent aggregate P3HT in the films.[29] The absorption model is applied to the absorbance data given in Figure 1, with the best fit values of W and σ, as well as the estimate of percent aggregate given in Figure 2a–c. Details of the model are provided in the Supporting Information. It was found that while the aggregates align in the direction of strain, the overall percent aggregate does not change appreciably with strain. For the aggregates aligned primarily in the direction of strain, annealing the film increased the aggregate quality (decrease in σ) significantly while the average conjugated length increased (decrease in W) slightly. For aggregates aligned primarily perpendicular to the strain direction, annealing the strained films decreases both the aggregate quality and conjugation length. This result may arise from increased alignment

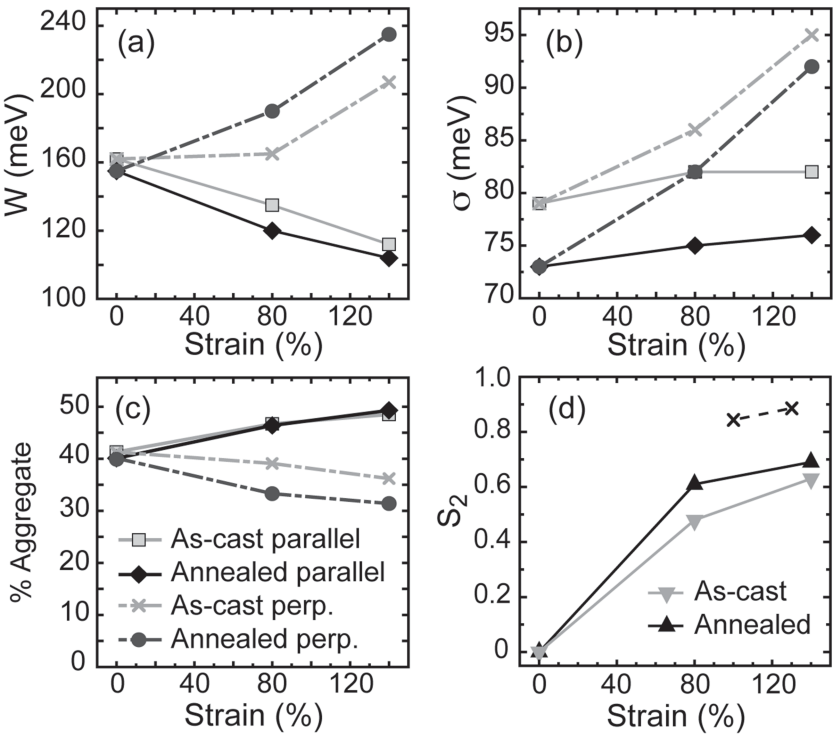

Figure 2. a,b) Weakly coupled H-aggregate absorption model parameter fits of strained P3HT films: a) free-exciton bandwidth (W), b) the Gaussian linewidth (σ). c) The estimated percent aggregate for strained as-cast and annealed P3HT films. Aggregate fraction estimated with polarized light and thus accounting for ≈1/2 of the amorphous material. d) 2D order parameter for as-cast and annealed films. The Δ symbols are the ordered parameters obtained from absorbance measurements ($S_{2,mol}$) and the x symbols are the order parameters obtained from the X-ray ϕ-scans ($S_{2,cryst}$) for annealed films. Annealing conditions were 180 °C for 10 min.

of the more ordered, initially misaligned regions of the film, in agreement with the increase observed in $S_{2,mol}$ with annealing.

Grazing incidence X-ray diffraction (GIXD) was used to probe the crystalline P3HT packing characteristics. Two-dimensional GIXD images are given in **Figure 3** for films strained by 140% as-cast, and after thermal annealing at 200 °C. The images are with the X-ray beams parallel and perpendicular (scattering vector nominally perpendicular and parallel, respectively) to the strain direction for each film. The as-cast film shows highly anisotropic scattering behavior similar to that previously reported.[1] The P3HT crystallites with the polymer long-axis aligned in the direction of strain have a broad out-of-plane stacking distribution with preferential bimodal character consisting of both face-on (conjugated ring plane parallel to the substrate) and edge-on (conjugated ring plane perpendicular to the substrate) stacking. When the strained film is annealed at 200 °C these aligned crystals show a sharper bimodal character. In addition, when the X-ray beam is incident perpendicular to the strain direction, mixed index scattering peaks of the annealed film become significantly more intense as compared to the as-cast film. Additional details are provided by high-resolution in-plane GIXD line scans shown in **Figure 4**. It is observed that thermally annealing the film at 200 °C significantly increases the sharpness and intensity of the in-plane scattering peaks for the scattering vector parallel and perpendicular to the strain direction. The scattering intensity increases for both (h00) and (0l0) suggesting that out-of-plane packing remains similar with annealing; however, the crystallite size and/or quality increases significantly. Finally, the (200) peak scattering intensity with azimuthal angle (ϕ) is given in Figure 4b for an as-cast film strained by 112%, and thermally annealed films strained to 100% and 130%. It is seen that the scattering intensity increases for the annealed films, consistent with the in-plane line scan. A 2D order parameter for the crystalline P3HT is given by $S_{2,cryst} = 2\langle\cos^2(\phi)\rangle - 1$. This order parameter can be shown to have the same origin and limits as the $S_{2,mol}$, but only considers the orientation of the P3HT crystallites (additional details provided in the Supporting Information).[1] It is found that $S_{2,cryst} = 0.84$ for the 112% as-cast film, $S_{2,cryst} = 0.85$ for the 100% strained annealed film, and $S_{2,cryst} = 0.89$ for the 130% strained annealed film. These values were calculated by subtracting an approximate background scattering intensity, as given in Figure 4b. The uncertainty in the order parameter is expected to be similar to $S_{2,mol}$. Assuming that the out-of-plane stacking is consistent with azimuthal angle, $S_{2,cryst}$ can be taken as the crystalline P3HT order in the film. We find that the crystallites of the highly strained as-cast films are well aligned in the direction of strain, and annealing the films only increases the order parameter slightly.

To determine morphological features at a larger length scale, we measured the structural characteristics of strained films using GI-SAXS and TEM. **Figure 5** shows GI-SAXS scattering for as-cast and annealed films strained by 140% with the scattering vector parallel and perpendicular to the strain direction. No scattering peak is observed for the as-cast film, however when annealing the film at 180 °C, a scattering peak appears at approximately 0.43 nm^{-1} for the scattering vector parallel to the strain direction. This peak is indicative of a characteristic periodicity in the film of approximately 15 nm. To gain a clearer picture of these features, films strained by 140% were investigated with TEM, with characteristic images given in Figure S1, Supporting Information. The dark-field TEM image after annealing shows the formation of weakly visible small aspect ratio fibrils aligned perpendicular to the strain direction that correspond well to the scattering peak observed in the GI-SAXS. These fibrils are similar in width to fibrils previously observed in low-molecular weight P3HT films.[31,32] For the 140% strain annealed films, the exciton bandwidth of the aggregates is approximately 110 meV, which corresponds to roughly 30 thiophene repeat units or 12 nm in length.[30] This length corresponds well to the GI-SAX scattering behavior suggesting that the fibrils are composed of P3HT aggregates. Finally, atomic force microsopy (AFM) measurements were performed on the strained films, with results given in Figure S2 (Supporting Information), however no fibril features were observed.

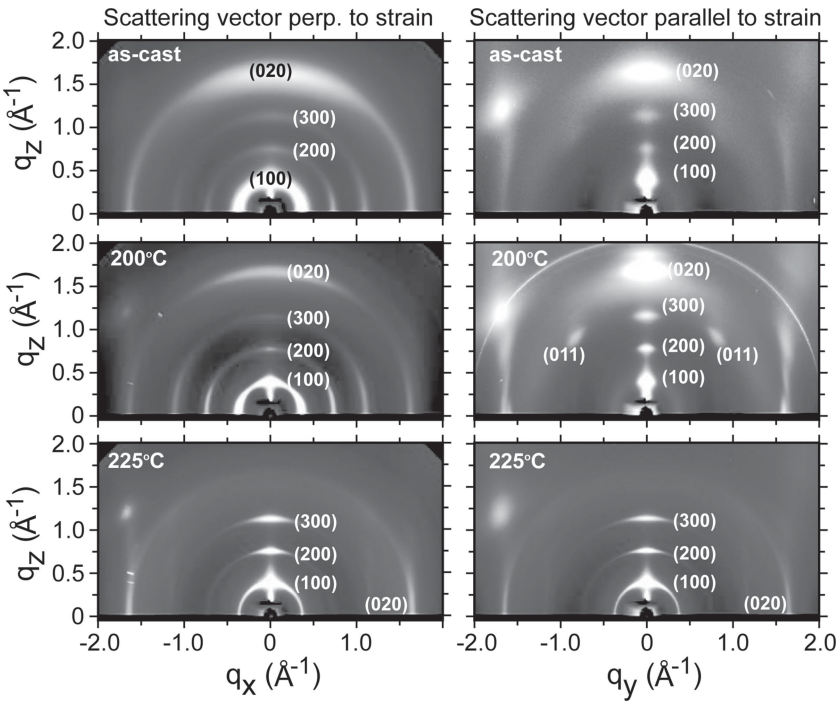

Figure 3. 2D-GIXD images for films strained by 140%. The images on the left are for the X-ray beam parallel to the strain direction (scattering vector nominally perpendicular to the strain direction). The images on the right are for the X-ray beam perpendicular to the strain direction (parallel scattering vector). The films are measured as-cast and thermally annealed at 200 °C as given in each image.

Comparing the results from the various characterization tools allows for several important morphological features to be resolved. We find that straining the P3HT films aligns the polymer long-axis in the direction of strain. The crystalline domains with the polymer long-axis aligned in the direction of strain have a bimodal orientation preference with both face-on and edge-on packing. The percentage of aggregate P3HT in the strained films increases slightly for both as-cast and thermally annealed films. Annealing the strained films improves alignment and average conjugation length slightly, but has a more significant influence on increasing the quality of the aggregate P3HT with backbones aligned in the direction of strain. The increase in P3HT aggregate quality coincides with the formation of fibrillar P3HT grains aligned perpendicular to the strain direction. The fibrils have relatively well-defined widths as measured by TEM and GI-SAXS (≈15 nm), and are similar to the estimated aggregate length measured with UV-Vis (≈12 nm). Therefore the fibrils are believed to be composed of P3HT aggregates with the polymer backbone aligned along the fibril short axis direction. The fibrils appear to be relatively short (ratios of 1:3) and variable in length.

2.2. Field Effect Charge Mobility

The macroscale in-plane charge transport in the films was studied in a bottom gate, bottom contact, thin-film transistor configuration with a focus on the saturated field effect mobility. In our previous study of uniaxially strained P3HT films, high mobility anisotropy was reported with the saturated field effect mobility increasing parallel to the strain direction and decreasing in the transverse direction.[1] In these films there is a slight channel length dependence that we attribute to the field dependence of the charge mobility and do not believe this is due to contact resistance.[33] Annealing the aligned films decreases the field effect mobility for transport both parallel and perpendicular to the strain direction, as shown in **Figure 6**. The reduction in mobility is more severe for transport parallel to the strain direction, resulting in a large drop in mobility anisotropy also given in Figure 6. To determine the evolution of the drop in mobility with thermal annealing, the field effect mobility parallel to the strain direction for a 140% strained film under varying annealing temperatures is given in **Figure 7**. It is observed that the mobility increases slightly at a low anneal temperature of 80 °C, but decreases continuously with further increases in annealing temperature. Within this entire temperature range, P3HT is above its glass transition temperature and below its melting temperature,[34,35] and the film microstructure likely evolves to greater extents with increasing anneal temperature.

To determine if there is a unique energetic barrier to charge transport between the thermally annealed and as-cast films, the temperature dependence of the field effect mobility for the 140% strained as-cast and annealed films is given in **Figure 8**. The mobility in the temperature range of 300 K to 150 K is fit to an Arrhenius type transport behavior, $\mu = \mu_0 \exp(-E_A/K_bT)$, where E_A is the activation energy, μ_0 is the mobility prefactor, and K_b is the Boltzmann constant.[22] The activation energy and mobility prefactor values for the films are tabulated in Figure 8, with the uncertainty given as the standard error in the exponential fit. The E_A of the films are found to be similar with a slight but statistically significant decrease after thermal annealing the film. The similar temperature dependence suggests that transport in each direction has a similar transport bottleneck, which can be attributed to the disordered regions of the films.

2.3. Time-Resolved Microwave Conductivity

Field effect mobility measurements sample charge transport across the entire channel length, convoluting the influence of aggregates, disordered regions, and the boundaries between these domains. Thus, even with the detailed structural analysis described above, it is impossible to discern the relative importance of specific structural features to charge transport without a complimentary technique. To address this problem we use flash-photolysis time resolved microwave conductivity (TRMC) to probe the average microscopic mobility anisotropy. Due to the high frequency (9 GHz) and low electric field

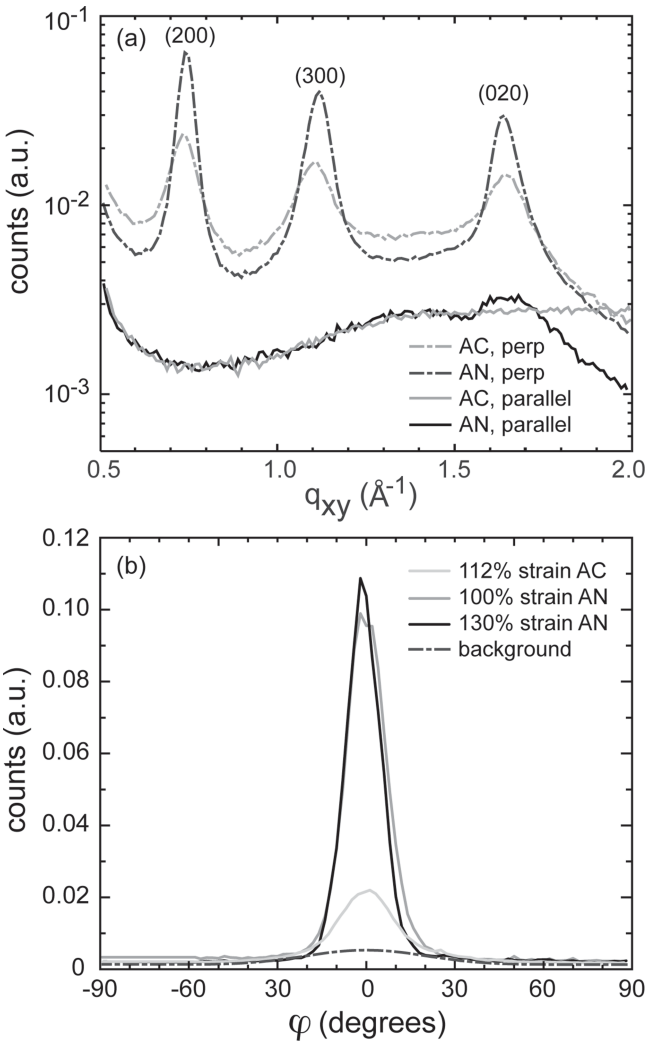

Figure 4. a) GIXD in-plane line-scan of 140% strained films, with scattering vector parallel and perpendicular (perp) to the strain direction for as-cast (AC) and thermally annealed (AN) at 180 °C for 10 min. b) GIXD ϕ-scans of the (200) peak for several strained films both as-cast and thermally annealed. The films are under different strains, nevertheless, annealing is shown to strongly increase scattering intensity.

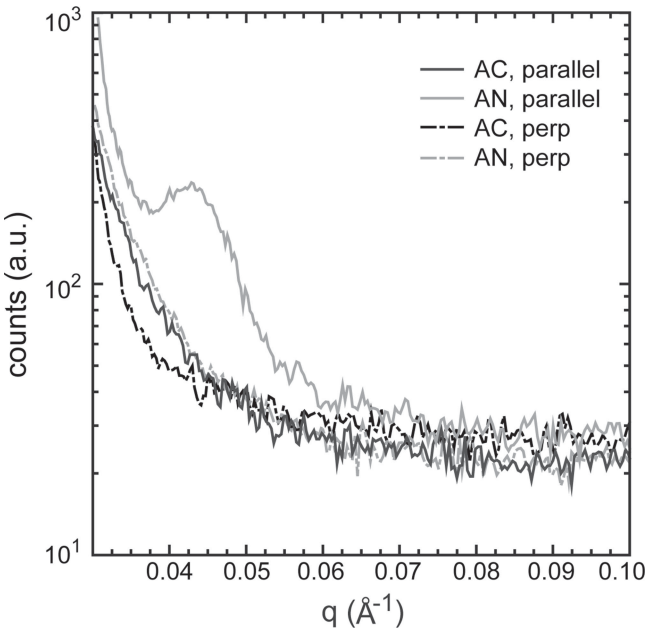

Figure 5. GI-SAXS data for 140% strained films with scattering vector parallel and perpendicular to the strain direction. One film is left as-cast (AC) and the other is annealed (AN) at 200 °C for 5 min prior to data collection.

strength (≈100 V cm^{-1}) used in this measurement, the microwave probe merely perturbs the random diffusive motion of charges, sampling local mobility without forcing carriers to traverse unfavorable paths.[36] The TRMC measurement and data analysis are described in detail elsewhere.[37–40] Briefly, the sample is mounted at one electric field maximum of a rectangular TE_{102} microwave cavity tuned to ≈9 GHz. The continuous microwave probe beam (≈100 mW), is polarized along the short axis of the rectangular cavity cross-section. We measure the time-resolved photoconductance of the sample in response to a short (4 ns) polarized laser pulse by monitoring the change in microwave power absorbed in the sample. The resulting photoconductance transients are fit using a sum of three exponential functions convoluted with the response function of the cavity,[37] and the sum of the exponential pre-factors is used to estimate the initial photoconductance, accounting approximately for any trapping or recombination that takes place during the laser pulse, as well as for the smoothing of the transient at early times due to the finite (ca. 10 ns) response time of the microwave cavity. From the initial photoconductance we calculate the product of charge carrier yield (ϕ) and the sum of charge density-weighted average mobility of electrons and holes, $\Sigma\mu$ (= μ_e + μ_h), where μ_e is the density-weighted average electron mobility and μ_h is the density-weighted average hole mobility.[37]

Without an external measure of either yield or GHz-frequency mobility sum, neither can be quantified independently. However, by maintaining equivalent sample excitation conditions, and thus nominally constant carrier yield, we obtain quantitative values for the GHz mobility anisotropy in the strain-oriented films. We performed TRMC measurements both with the microwave electric field parallel and orthogonal to the axis of strain, while maintaining a constant relationship between the optical pump polarization and strain orientation. Conversely, we can obtain quantitative values for the anisotropy in carrier yield by measuring the ratio of $\phi\Sigma\mu$ for excitation polarization parallel and orthogonal to the strain direction, while maintaining a constant microwave probe polarization. The various laser pump (E_P) – film (S) – microwave probe (E_{GHz}) orientations are schematically provided in the inset of **Figure 9**. Figure 9a shows the GHz mobility anisotropy for films strained to 50% and 100%, both in as-cast and annealed condition. We find that the GHz mobility anisotropy increases with strain, and decreases with annealing. These results were found to be independent of optical pump orientation relative the axis of strain. Figure 9b shows the yield anisotropy ratio; exciting the polymer parallel to the strain axis provides a lower yield of charge carriers than when exciting with orthogonal polarization. We expect the photoconductance signal to be dominated by holes in the crystallites, irrespective

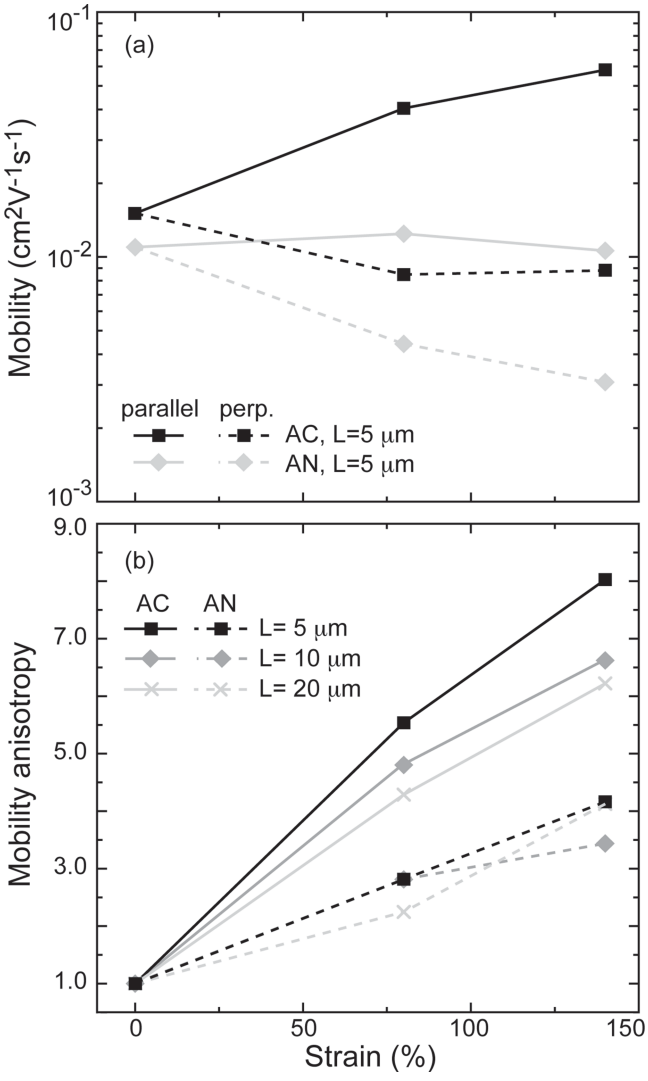

Figure 6. a) Field-effect mobility for films transferred without strain, strained by 80% and by 140% for as-cast (AC) and thermally annealed (AN) conditions (180 °C for 5 min). The mobility is given for channel lengths of 5 μm, with data for 10 μm channel lengths provided in the Supporting Information. b) The mobility anisotropy for transport parallel relative to transport perpendicular to the strain direction. The mobility anisotropy is given for OTFT channel lengths of (5, 10, and 20) μm.

of absorption location. It has been shown that the generation of free long-lived (lifetimes ≥ 10 ns) charge in neat conjugated polymers is dominated by the interface between crystalline and amorphous domains, resulting in a microwave photoconductance signal dominated by holes (for p-type polymers such as P3HT) injected into the crystallites.[37] This suggests that the observed yield anisotropy may be due to a difference in the location of light absorption in the material, altering the proximity of excitons to defects and grain boundaries that assist exciton dissociation.[37–41] When the excitation pulse is polarized parallel to the strain direction absorption in the oriented crystallites will be favored, whereas the orthogonal polarization will favor absorption in the remaining disordered or unaligned regions of the film.

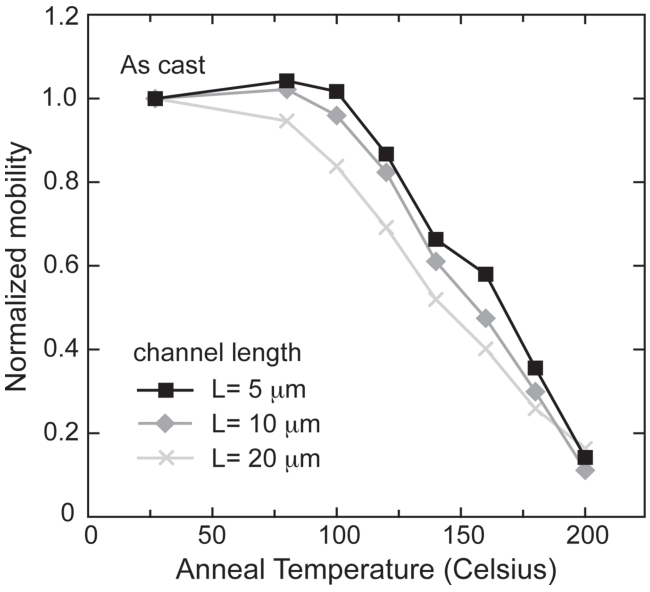

Figure 7. Normalized saturated field effect mobility parallel to the strain direction for a series of 140% strained films under various thermal-annealing temperatures. The normalization is made by measuring the mobility of the film in its as-cast condition relative to the mobility after annealing for 10 min at the given temperature.

	AC para	AC perp	AN para	AN perp
E_A (meV)	77+/-4	92+/-6	64+/-10	81+/-7
μ_0 (cm^2/Vs)	0.46+/-.08	0.13+/-.03	0.07+/-.03	0.03+/-.01

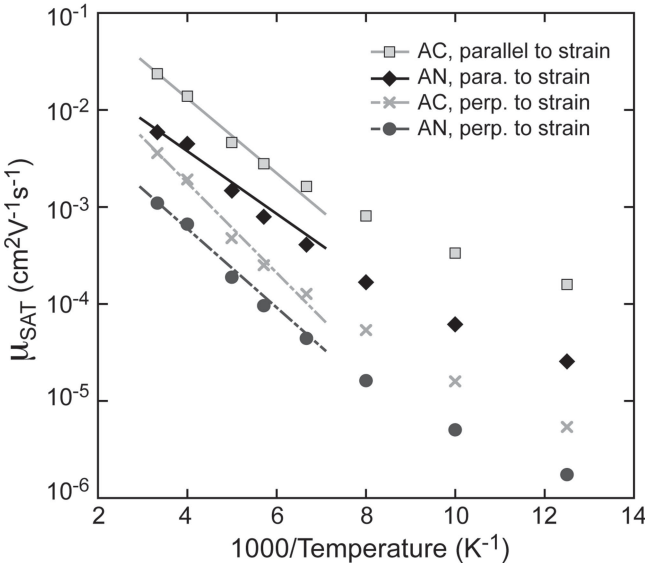

Figure 8. The temperature dependence of the field-effect mobility for 4 films all strained by 140%. Two films are as-cast (AC), one with strain parallel to the channel, one perpendicular. Two films are annealed (AN) at 180 °C 10 min, one with strain parallel to the channel, one perpendicular. Two 10-um channel length transistors are tested per film. The solid lines are fit using $\mu = \mu_0 \exp(-E_A/K_bT)$, where E_A is the activation energy, μ_0 is the mobility prefactor, and K_b is the Boltzmann constant. The fit is over the first 5 higher temperature data points with values tabulated above the plot.

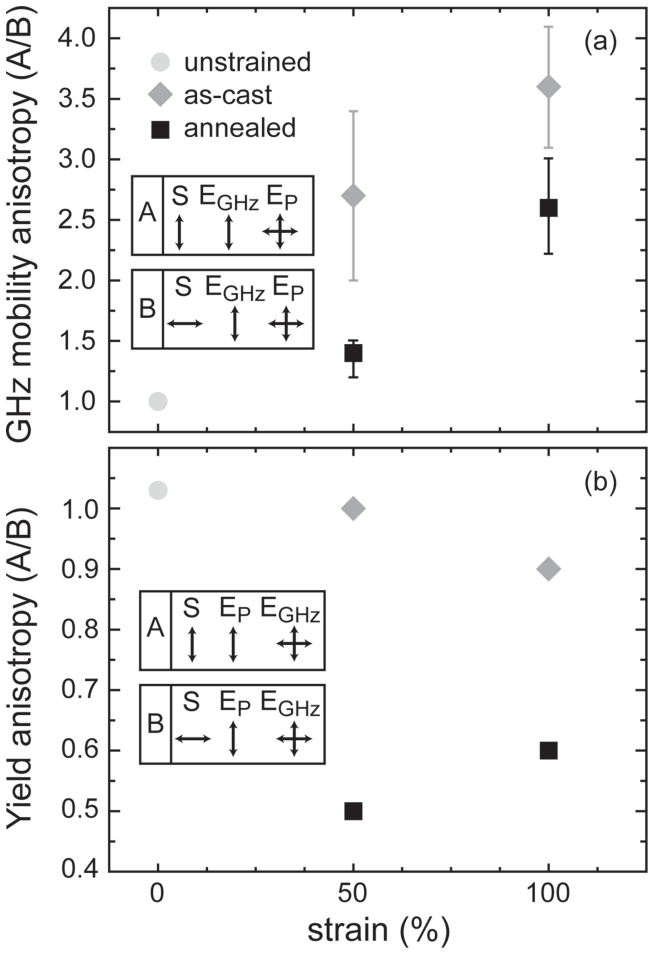

Figure 9. a) TRMC mobility anisotropy as a function of strain and annealing. b) TRMC yield anisotropy as a function of strain and annealing (180 °C for 10 min). Anisotropy values are obtained by dividing the $\phi\Sigma\mu$ value obtained at low pump intensity for the polarization parallel to the axis of strain in the sample (A) by that obtained with the orthogonal polarization (B): $(\phi\Sigma\mu)_A/(\phi\Sigma\mu)_B$. The mobility anisotropy is obtained by varying the microwave probe polarization relative to the strain axis while maintaining constant pump polarization. The data is for an average of the two possible pump orientations. Conversely, the yield anisotropy is obtained by varying the pump polarization relative to the strain axis while maintaining constant probe polarization, and taking an average of the data for the two possible probe orientations. The relative orientations of the film strain alignment direction (S), laser pump (E_P), and microwave probe (E_{GHz}) is given in the inset. The two crossed arrows indicate that the measurements were taken in both possible orientations and averaged. The black circle in (a) is defined as 1 and provided as a guide to the eye. The black circle in (b) is an experimental data point. The indicated error bar in (a) is the estimated standard deviation of the mean.

3. Discussion

In our previous study of as-cast, strain aligned films,[1] we found significant orientation of the crystalline regions with the polymer chain axis oriented along the strain direction, moderate orientation of the entire film from UV-Vis and slight changes in the excitonic bandwidth (optical order). The most surprising observation was the development of a significant crystalline population that was face-on, in contrast to the nearly complete edge–on orientation of the initially spin-coated film. The development of significant anisotropy in the morphology was accompanied by the emergence of significant anisotropy in the OTFT mobility. The macroscopic mobility increased by ≈ a factor of 2 along the strain direction, and an anisotropy of up to 9 at 140% strain was observed. The increase in mobility along the strain direction was taken as clear evidence that the anisotropy was not attributable to significant cracks (or other major defects) from the strain process.

In the current study, we find that moderate thermal anneals (below the melting point) result, in general, in small improvements in the orientational and aggregate order. In addition, there does not appear to be a significant change in the population of face-on material. The most significant morphological change upon annealing is the development of a distinct morphology of ≈15 nm wide fibrils oriented perpendicular to the strain direction. The development of fibrils strongly suggests ripening of the initial ordered regions due to removal of chain defects and tie-chain pull-out. This is consistent with the known behavior of semicrystalline high molecular weight polymers, where crystalline tie-chains are largely formed during primary crystallization.[42] Subsequent annealing can improve aggregate quality, but an increase in the number of tie-chains chains does not typically occur. In fact, aggregate quality may improve at the cost of tie chain removal.[43]

In contrast with the small morphological changes observed upon annealing, the OTFT mobility is observed to change dramatically upon annealing, with a nominal reduction by a factor of 4 in the strain direction, a reduction by a factor of 2 in the perpendicular direction, and a concomitant (2×) decrease in the anisotropy. As virtually all local measures of order (exciton bandwidth, GIXD intensity) and orientation (S_2) increase upon annealing, the drop in macroscopic transport is attributed to loss of intergain connectivity due to tie-chain pull out. Thus, a large portion of the observed mobility in aligned as-cast films is attributed to favorably aligned tie-chains, in agreement with the generally accepted hypothesis that grain boundaries are crucial to transport in semicrystalline polymers.[22,25] Tie-chain removal greatly reduces favorable percolation pathways for charge transport and reduces the field effect mobility in the polymer long-axis alignment direction. The average polymer chain length for the P3HT used in this study (≈120 nm) is much longer than an individual fibril width (≈15 nm), suggesting that a given polymer chain may traverse a number of aggregates separated by disordered domains. Thus, it is unlikely that all tie-chains are removed, and the remaining chains may actually improve in local order and alignment, resulting in the small decrease in activation energy observed in the low-temperature OTFT measurements. The second, and more important, implication of the observed changes in macroscale mobility with annealing is that transport due to tie chains in the as-cast material must be significantly anisotropic. Using estimates for the aggregate fraction of the film to be ≈0.4 and assuming the aggregate P3HT does not deviate substantially from the angular distribution of the crystalline P3HT, the anisotropy in the UV-Vis relative to the GIXD suggests that the disordered material still exhibits an S_2 of ≈0.56 (addition details provided in the Supporting Information). This is consistent with simple connectivity arguments for tie chains between oriented aggregates. In recent quantum-chemical

studies of transport in the inter-grain regions, it was found that intrachain transport along "bridging" (tie) chains is facile (mobility comparable to that along the chain axis on grain) while interchain transport was significantly slower.[18]

The surprising observation in this study is that of a small anisotropy in TRMC measurements. The microwave photoconductance is expressed as the product of charge carrier yield and mobility ($\phi\Sigma\mu$) as previously described. Thus, the technique will strongly favor the most ordered (highest μ) regions, and intrachain mobility is expected to be much higher than interchain mobility, even within crystallites. Furthermore, the carrier mobility along the lamella stacking direction should be extremely small due to poor electronic coupling.[18] This means that while both the face-on and edge-on crystallites will contribute photoconductance signal from intrachain transport, only the edge-on aggregates are oriented properly for probing the intermolecular transport (i.e., along the π–π stacking direction). Therefore the TRMC anisotropy will overestimate the anisotropy associated with transport along the chain vs. transport along the π–π stacking direction for bimodal out-of-plane stacking films as found in the aligned films in this study. Despite these considerations, we find that the TRMC mobility anisotropy is quite small, 3.5 at most for a 100% strained film. Between the considerations outlined above and the relatively large effective mass (low bandwidth) estimated in the π–π stacking direction[19] this low anisotropy is very surprising. In recent studies of rigid, ladder polymer oligomers it was observed that TRMC could produce artificially low estimates of the mobility when the grain ends are probed during the microwave cycle. This effect results in a strong grain size dependence to the extracted mobility.[44,45] However, in a recent pulse radiolysis-TRMC study of P3HT as a function of molecular weight, no strong crystal size dependence was observed in μ.[46] We estimate that the scattering length of carriers will be on the order of 10 nm,[46–48] and thus the local μ is accurately reflected in the present data and the anisotropy is small. We suggest the low anisotropy arises from the extremely low energy barrier to torsional disorder in the relatively flexible P3HT, limiting mobility along the chain axis. This is consistent with the similar activation energies reported for OTFT and local mobility from PR-TRMC in unstrained films.[46] An additional minor contribution to the small anisotropy is believed to be due to low-order aggregates not aligned in the direction of strain that remain efficient intramolecular transport paths. These aggregates may not diffract significantly but do have weak vibronic character as observed in the absorbance and contribute to the difference observed in order parameters $S_{2,\mathrm{mol}}$ and $S_{2,\mathrm{cryst}}$. The reduction in the local mobility anisotropy with thermal annealing occurs while the alignment is shown to increase and is thus attributed to the improved aggregate quality, favoring improved transport in the π–π stacking direction to a greater extent than the backbone direction.

In summary, the high bulk mobility anisotropies demonstrated in conjugated semicrystalline polymers, such as P3HT, are likely due to intergrain morphological features, in particular favorably aligned tie chains that couple well orientated aggregates. The local GHz-mobility anisotropy is lower than the macroscopic mobility anisotropy, believed to be due to local polymer disorder along the P3HT backbone direction being a limiting factor.

4. Experimental Section

Film Preparation: P3HT was purchased from Plextronics Inc. with a number-averaged molecular mass M_n = 50 kDa, a regioregularity of 99%, and a polydispersity of 2.1.[49] The P3HT solution is dissolved in Chloroform at 8 mg/ml and heated for a minimum of 4 h at 75 °C. The films are spin coated at 104.7 rad s^{-1} (1000 rpm) onto octyltrichlorosilane (OTS) treated Si for 45 s at room temperature in a Nitrogen filled glove box. Strained films are prepared by first laminating PDMS onto the cast P3HT films and removing the PDMS quickly resulting in the P3HT film adhering to the PDMS slab and being fully removed from the OTS-silicon substrate. The P3HT-PDMS stack is strained, plastically deforming the P3HT. These strained P3HT films are then laminated onto a secondary substrate and the PDMS is removed. Unstrained films are prepared in the same manner without straining the P3HT-PDMS stack. Final substrates include glass, fused quartz, and OTS-silicon with a native or thermal oxide layer. All substrates are cleaned with sonication in acetone, isopropanol, and DI water followed by UV ozone treatment. The OTS treated silicon consists of immersing the cleaned silicon substrates in a 0.002 mol L^{-1} solution of OTS in anhydrous hexadecane for 12 h to 16 h followed by sonication in chloroform, isopropanol, and deionized (DI) water. The substrate is then heated on a hot-plate at 150 °C for 10 min followed by DI water rinse. PDMS was prepared by mixing the elastomer with the cross linker at a ratio of 15:1 and heating for 14 h at 60 °C. The PDMS base to cross linker ratio was chosen to maximize the strain limit of the elastomer.

Morphology Characterization: The UV–vis absorbance measurements were performed with a Perkin Elmer Lambda 950 UV–visible-near-IR spectrometer. The absorbance was measured for films on glass substrates with the absorbance of a clean glass reference substrate subtracted from the data. X-ray diffraction measurements were performed at the Stanford Synchrotron Radiation Lightsource (SSRL) on beam lines 7–2 and 11–3. The point detector GIXD measurements were conducted on beam line 7–2. The films were illuminated with an 8 keV beam at a constant incidence angle of approximately 0.2°. The sample in-plane orientation relative to the beam was adjusted at each q-value to maintain the scattering vector parallel or perpendicular to the strain direction. For ϕ-scans, the sample tilt was adjusted to make the sample normal collinear with the rotation axis of the ϕ motor and maintain a constant incidence angle as the sample was rotated. The 2D GIXD measurements were conducted on beam line 11–3 with an area detector (MAR345 image plate), an energy of 12.735 keV, and an incidence angle of ≈0.12°. For area detector measurements, the samples were aligned with their in-plane orientation either perpendicular or parallel to the incident beam. This orientation resulted in the scattering vector being aligned away from the strain direction by θ_B. For the energy used, θ_B was 3.3° for the (200) and 7.3° for the (010) scattering peaks, both less than the FWHM observed in the ϕ-scans. All sample chambers were purged with helium during the scattering experiments to reduce beam damage and background scattering. The GI-SAXS measurements were performed at the X-9 beamline at the National Synchrotron Light Source, Brookhaven National Laboratory. The incident X-ray beam (E = 14 keV) was collimated using slits and focused onto the sample position using Kirkpatrick-Baez mirrors. The samples and beam path were in vacuum. The TEM measurements were made with a Philips EM400T transmission electron microscope, operated at 120 kV. For TEM sample preparation, a thin layer of carbon (≈10 nm) was deposited onto the strained P3HT film supported by Si wafer. A poly(acrylic acid) (PAA) aqueous solution (20% by mass) was then drop-cast on top of the carbon-coated film and heated overnight at 55 °C. The dried PAA was removed from the substrate taking along the P3HT film underneath. The delaminated film was floated on water for ≈3 h until PAA was dissolved away, and then picked up with a blank TEM copper grid. The retrieved specimen was rinsed with water prior to imaging.

Electrical Characterization: The OTFT transistors were bottom gate, bottom contact transistors where the gate electrode was a highly doped p-type silicon that also acted as the device substrate. The gate dielectric was a 300 nm thermal oxide layer and the source drain electrodes

consisted of a 5 nm Ti wetting layer followed by 40 nm Au. The test-beds were OTS treated as described above. The P3HT films were then printed onto the test structures to complete the device. The channel widths for all devices were 1000 µm while the channel lengths included (5, 10, and 20) µm. The transistors were measured using an HP 4156b parameter analyzer in an argon filled glove box. Room-temperature TFTs were measured in the saturated regime by sweeping the gate voltage (V_G) from 20 V to –70 V, with a source–drain voltage (V_{SD}) of –70 V. Low-temperature measurements were performed with a Desert Inc. cryogenic probe station in the saturation regime, with V_G swept from 20 V to –70 V and V_{SD} = –60 V. Low-temperature measurements were conducted at a pressure of approximately 1.3×10^{-6} Pa (10^{-8} Torr). The saturated field-effect hole mobility was calculated from a linear fit of $I_{SD}^{1/2}$ versus V_G, where I_{SD} is the source-drain current. In room temperature measurements, the mobility was taken as an average of a minimum of 4 devices. The low temperature mobility values are from an average of 2 devices. In the TRMC measurements, the film is excited with a polarized 4 ns FWHM laser pulse at $\lambda = 532$ nm using an OPO-Continuum Panther pumped with the 3rd harmonic of a Nd:YAG laser: Continuum Powerlite. The polarization of the laser pulse was purified using a quartz beam splitting cube, and the polarization axis controlled via a quarter-wave plate. Microwave absorption originates from the non-resonant interaction of mobile photogenerated charges in the sample with the microwave electric field. Samples are mounted at the electric-field maximum of an X-band TE_{102} microwave resonance cavity tuned to 9 GHz, which increases sensitivity at the expense of time resolution due to the ring-down time of the cavity (≈10 ns). All samples were stored and measured under nitrogen. All of the TRMC data reported here were derived from fits to the photoconductance transients using a triple-exponential function convoluted with the instrument response function, the latter of which is modeled using a Gaussian laser pulse convoluted with the (known) single exponential decay time of the microwave cavity. The experimental setup and data analysis procedures are documented in detail elsewhere.[37–40]

Supporting Information

Supporting Information is available from the Wiley Online Library or from the author.

Acknowledgements

The authors thank Kevin Yager for assistance with the GI-SAXS measurements. Portions of this research were carried out at the Stanford Synchrotron Radiation Lightsource, a Directorate of SLAC National Accelerator Laboratory and an Office of Science User Facility operated for the U.S. Department of Energy Office of Science by Stanford University. Research was carried out in part at the Center for Functional Nanomaterials, Brookhaven National Laboratory, which is supported by the U.S. Department of Energy, Office of Basic Energy Sciences, under Contract No. DE-AC02–98CH10886. The TRMC system described here, was funded by the Solar Photochemistry Program, Division of Chemical Sciences, Geosciences, and Biosciences, Office of Basic Energy Sciences, U.S. Department of Energy. Portions of the experimental work were supported by the Laboratory Directed Research and Development (LDRD) Program at the National Renewable Energy Laboratory under task number 06RF1002. Work conducted at NREL was supported by the U.S. Department of Energy under Contract No. DE-AC36–08-GO28308 with the National Renewable Energy Laboratory. B. O'Connor would like to acknowledge NIST/NRC post-doctoral fellowship and support of this work by the National Science Foundation under Grant No. CMMI-1200340.

Received: September 28, 2013
Revised: December 20, 2013
Published online: February 18, 2014

[1] B. O'Connor, R. J. Kline, B. R. Conrad, L. J. Richter, D. Gundlach, M. F. Toney, D. M. DeLongchamp, *Adv. Funct. Mater.* **2011**, *21*, 3697–3705.
[2] H. R. Tseng, L. Ying, B. B. Y. Hsu, L. A. Perez, C. J. Takacs, G. C. Bazan, A. J. Heeger, *Nano Lett.* **2012**, *12*, 6353–6357.
[3] D. M. DeLongchamp, R. J. Kline, Y. Jung, D. S. Germack, E. K. Lin, A. J. Moad, L. J. Richter, M. F. Toney, M. Heeney, I. McCulloch, *ACS Nano* **2009**, *3*, 780–787.
[4] H. Sirringhaus, R. J. Wilson, R. H. Friend, M. Inbasekaran, W. Wu, E. P. Woo, M. Grell, D. D. C. Bradley, *Appl. Phys. Lett.* **2000**, *77*, 406–408.
[5] J. Rivnay, L. H. Jimison, J. E. Northrup, M. F. Toney, R. Noriega, S. F. Lu, T. J. Marks, A. Facchetti, A. Salleo, *Nat. Mater.* **2009**, *8*, 952–958.
[6] M. J. Lee, D. Gupta, N. Zhao, M. Heeney, I. McCulloch, H. Sirringhaus, *Adv. Funct. Mater.* **2011**, *21*, 932–940.
[7] C. W. Sele, B. K. C. Kjellander, B. Niesen, M. J. Thornton, B. P. H. van der Putten, K. Myny, H. J. Wondergem, A. Moser, R. Resel, A. J. J. M. van Breemen, N. van Aerle, P. Heremans, J. E. Anthony, G. H. Gelinck, *Adv. Mater.* **2009**, *21*, 4926.
[8] S. H. Jin, H. U. Seo, D. H. Nam, W. S. Shin, J. H. Choi, U. C. Yoon, J. W. Lee, J. G. Song, D. M. Shin, Y. S. Gal, *J. Mater. Chem.* **2005**, *15*, 5029–5036.
[9] C. Reese, Z. N. Bao, *Mater. Today* **2007**, *10*, 20–27.
[10] R. J. Li, L. Jiang, Q. Meng, J. H. Gao, H. X. Li, Q. X. Tang, M. He, W. P. Hu, Y. Q. Liu, D. B. Zhu, *Adv. Mater.* **2009**, *21*, 4492.
[11] L. Hartmann, K. Tremel, S. Uttiya, E. Crossland, S. Ludwigs, N. Kayunkid, C. Vergnat, M. Brinkmann, *Adv. Funct. Mater.* **2011**, *21*, 4047–4057.
[12] L. Biniek, N. Leclerc, T. Heiser, R. Bechara, M. Brinkmann, *Macromolecules* **2013**, *46*, 4014–4023.
[13] V. C. Sundar, J. Zaumseil, V. Podzorov, E. Menard, R. L. Willett, T. Someya, M. E. Gershenson, J. A. Rogers, *Science* **2004**, *303*, 1644–1646.
[14] F. Ortmann, F. Bechstedt, K. Hannewald, *Phys. Status Solidi B* **2011**, *248*, 511–525.
[15] E. J. W. Crossland, K. Tremel, F. Fischer, K. Rahimi, G. Reiter, U. Steiner, S. Ludwigs, *Adv. Mater.* **2012**, *24*, 839.
[16] Z. J. Zheng, K. H. Yim, M. S. M. Saifullah, M. E. Welland, R. H. Friend, J. S. Kim, W. T. S. Huck, *Nano Lett.* **2007**, *7*, 987–992.
[17] Y. Hosokawa, M. Misaki, S. Yamamoto, M. Torii, K. Ishida, Y. Ueda, *Appl. Phys. Lett.* **2012**, *100*, 203305.
[18] Y.-K. Lan, C.-I. Huang, *J. Phys. Chem. B* **2009**, *113*, 14555–14564.
[19] J. E. Northrup, *Phys. Rev. B* **2007**, *76*, 245202.
[20] L. H. Jimison, M. F. Toney, I. McCulloch, M. Heeney, A. Salleo, *Adv. Mater.* **2009**, *21*, 1568.
[21] B. H. Hamadani, D. J. Gundlach, I. McCulloch, M. Heeney, *Appl. Phys. Lett.* **2007**, *91*, 243512.
[22] R. A. Street, J. E. Northrup, A. Salleo, *Phys. Rev. B* **2005**, *71*, 165202.
[23] D. M. DeLongchamp, R. J. Kline, D. A. Fischer, L. J. Richter, M. F. Toney, *Adv. Mater.* **2011**, *23*, 319–337.
[24] X. R. Zhang, L. J. Richter, D. M. DeLongchamp, R. J. Kline, M. R. Hammond, I. McCulloch, M. Heeney, R. S. Ashraf, J. N. Smith, T. D. Anthopoulos, B. Schroeder, Y. H. Geerts, D. A. Fischer, M. F. Toney, *J. Am. Chem. Soc.* **2011**, *133*, 15073–15084.
[25] D. T. Duong, M. F. Toney, A. Salleo, *Phys. Rev. B* **2012**, *86*, 205205.
[26] M. C. Gurau, D. M. Delongchamp, B. M. Vogel, E. K. Lin, D. A. Fischer, S. Sambasivan, L. J. Richter, *Langmuir* **2007**, *23*, 834–842.
[27] F. C. Spano, *J. Chem. Phys.* **2005**, *122*, 234701.
[28] J. Clark, C. Silva, R. H. Friend, F. C. Spano, *Phys. Rev. Lett.* **2007**, *98*, 206406.
[29] J. Clark, J. F. Chang, F. C. Spano, R. H. Friend, C. Silva, *Appl. Phys. Lett.* **2009**, *94*, 163306.

[30] J. Gierschner, Y.-S. Huang, B. Van Averbeke, J. Cornil, R. H. Friend, D. Beljonne, *J. Chem. Phys.* **2009**, *130*, 044105.
[31] R. J. Kline, M. D. McGehee, *Polym. Rev.* **2006**, *46*, 27–45.
[32] R. Zhang, B. Li, M. C. Iovu, M. Jeffries-EL, G. Sauve, J. Cooper, S. J. Jia, S. Tristram-Nagle, D. M. Smilgies, D. N. Lambeth, R. D. McCullough, T. Kowalewski, *J. Am. Chem. Soc.* **2006**, *128*, 3480–3481.
[33] B. H. Hamadani, C. A. Richter, D. J. Gundlach, R. J. Kline, I. McCulloch, M. Heeney, *J. Appl. Phys.* **2007**, *102*, 044503.
[34] J. Y. Kim, D. Frisbie, *J. Phys. Chem. C* **2008**, *112*, 17726–17736.
[35] C. Mueller, T. A. M. Ferenczi, M. Campoy-Quiles, J. M. Frost, D. D. C. Bradley, P. Smith, N. Stingelin-Stutzmann, J. Nelson, *Adv. Mater.* **2008**, *20*, 3510.
[36] O. Hilt, L. D. A. Siebbeles, *Chem. Phys.* **1998**, *229*, 257–263.
[37] O. G. Reid, J. A. Malik Nekuda, G. Latini, S. Dayal, N. Kopidakis, C. Silva, N. Stingelin, G. Rumbles, *J. Polym. Sci. Part B* **2012**, *50*, 27–37.
[38] J. E. Kroeze, T. J. Savenije, M. J. W. Vermeulen, J. M. Warman, *J. Phys. Chem. B* **2003**, *107*, 7696–7705.
[39] A. J. Ferguson, N. Kopidakis, S. E. Shaheen, G. Rumbles, *J. Phys. Chem. C* **2008**, *112*, 9865–9871.
[40] M. P. DeHaas, J. M. Warman, *Chem. Phys.* **1982**, *73*, 35–53.
[41] L. J. Rothberg, M. Yan, F. Papadimitrakopoulos, M. E. Galvin, E. W. Kwock, T. M. Miller, *Synth. Met.* **1996**, *80*, 41–58.
[42] H. D. Keith, F. J. Padden, R. G. Vadimsky, *J. Appl. Phys.* **1971**, *42*, 4585.
[43] D. Ferrer-Balas, M. L. Maspoch, A. B. Martinez, O. O. Santana, *Polymer* **2001**, *42*, 1697–1705.
[44] F. C. Grozema, L. D. A. Siebbeles, *J. Phys. Chem. Lett.* **2011**, *2*, 2951–2958.
[45] F. C. Grozema, T. J. Savenije, M. J. W. Vermeulen, L. D. A. Siebbeles, J. M. Warman, A. Meisel, D. Neher, H. G. Nothofer, U. Scherf, *Adv. Mater.* **2001**, *13*, 1627.
[46] P. Pingel, A. Zen, R. D. Abellon, F. C. Grozema, L. D. A. Siebbeles, D. Neher, *Adv. Funct. Mater.* **2010**, *20*, 2286–2295.
[47] O. G. Reid, G. Rumbles, *J. Phys. Chem. Lett.* **2013**, *4*, 2348–2355.
[48] D. J. Bindl, A. J. Ferguson, M. Wu, N. Kopidakis, J. L. Blackburn, M. S. Arnold, *J. Phys. Chem. Lett.* **2013**, *4*, 3550–3559.
[49] Certain commercial equipment, or materials are identified in this paper in order to specify the experimental procedure adequately. Such identification is not intended to imply recommendation or endorsement by the National Institute of Standards and Technology, nor is it intended to imply that the materials or equipment identified are necessarily the best available for the purpose.